Mon. Not. R. Astron. Soc. **363,** 1299–1314 (2005) doi:10.1111/j.1365-2966.2005.09525.x

Effects of feedback on the morphology of galaxy discs

Takashi Okamoto,[1,2]★ Vincent R. Eke,[1] Carlos S. Frenk[1] and Adrian Jenkins[1]
[1]*Institute for Computational Cosmology, Department of Physics, University of Durham, South Road, Durham DH1 3LE*
[2]*Department of Theoretical Astronomy, National Astronomical Observatory Japan, Osawa, Mitaka, Tokyo 181-8588, Japan*

Accepted 2005 August 15. Received 2005 July 26; in original form 2005 March 30

ABSTRACT

We have performed hydrodynamic simulations of galaxy formation in a cold dark matter (ΛCDM) universe. We have followed galaxy formation in a dark matter halo, chosen to have a relatively quiet recent merger history, using different models for star formation and feedback. In all cases, we have adopted a multiphase description of the interstellar medium and modelled star formation in quiescent and burst modes. We have explored two triggers for starbursts – strong shocks and high gas density – allowing for the possibility that stars in the burst may form with a top-heavy initial mass function. We find that the final morphology of the galaxy is extremely sensitive to the modelling of star formation and feedback. Starting from identical initial conditions, galaxies spanning the entire range of Hubble types, with B-band disc-to-total luminosity ratios ranging from 0.2 to 0.9, can form in the same dark matter halo. Models in which starbursts are induced by high gas density (qualitatively similar to models in which feedback is produced by active galactic nuclei) generate energetic winds and result in galaxies with an early-type morphology. Models in which the starbursts are induced by strong shocks lead to extended discs. In this case, the feedback associated with the bursts suppresses the collapse of baryons in small haloes, helping to create a reservoir of hot gas that is available for cooling after $z \simeq 1$, following the bulk of the dynamical activity that builds up the halo. This gas then cools to form an extended, young stellar disc.

Key words: methods: numerical – galaxies: evolution – galaxies: formation.

1 INTRODUCTION

Understanding galaxy formation is a challenging problem whose solution will require a concerted approach combining observational, semi-analytical and numerical work. There have been substantial advances on all these fronts in the past decade, but fundamental questions remain unanswered. One of the most troublesome is the inability to produce realistic spiral galaxies in numerical simulations that start from initial conditions appropriate to the concordance cold dark matter cosmology (ΛCDM) and assume prescriptions for gas and stellar processes analogous to those included in semi-analytical models, or inferred directly from observations.

Pioneering N-body/gas-dynamical simulations by Katz & Gunn (1991), Navarro & Benz (1991) and Katz (1992) have already included many of the processes, which are generally regarded as essential for galaxy formation: radiative cooling, star formation, and feedback effects generated by energy released from associated with supernovae (SNe) and stellar winds. The simulations by Navarro & Benz (1991), and later by Navarro & White (1994) and Navarro, Frenk & White (1995), assumed CDM initial conditions. They uncovered a fundamental problem that prevents the formation of disc-dominated galaxies: the so-called 'angular momentum problem'. This is a generic problem that can be traced back to the very nature of the hierarchical clustering process characteristic of structure growth from CDM initial conditions (Frenk et al. 1985). At early times, small, dense CDM haloes form. Radiative cooling is very efficient and a large fraction of their gas, some of which will turn into stars, cools into their centres. As haloes merge to form larger objects, their orbital angular momentum is drained by dynamical friction and exported to the dark matter at the outskirts of the new haloes. Much of the original angular momentum of the baryonic material is lost and the resulting galaxies become too centrally concentrated.

Weil, Eke & Efstathiou (1998) and Eke, Efstathiou & Wright (2000) have shown that if cooling is artificially suppressed until the host haloes are well established, then the simulations can produce galaxies that are less centrally concentrated and have higher specific angular momenta. Two ways to prevent the early collapse of protogalactic clouds have been proposed: stronger feedback than that provided by standard treatments of SNe (Sommer-Larsen, Gelato & Vedel 1999; Thacker & Couchman 2001) and a modification of the cosmological framework, replacing CDM with warm dark matter (which does not induce small-scale fluctuations; Sommer-Larsen & Dolgov 2001; Governato et al. 2004). There are also indications that spurious numerical effects, arising from the very nature of the smoothed particle hydrodynamics (SPH) technique used in the

★E-mail: takashi.okamoto@durham.ac.uk

simulations, cause transfer of angular momentum from the cold gas disc to the hot halo gas, significantly contributing to the angular momentum problem (Okamoto et al. 2003). Aside from numerical effects, it is clear that the angular momentum problem in simulations is telling us something quite fundamental about the nature of star formation and feedback processes in galaxy formation.

Some recent simulations have yielded more promising disc galaxies in the CDM framework. Sommer-Larsen et al. (2003) were able to generate a variety of morphological types, including discs, by assuming a self-propagating star formation model combined with very efficient SNe feedback. In their model, star formation proceeds in two modes: 'early time' and 'late time'. In the early time mode, star formation is very efficient and the feedback is very strong; in the late time mode, the star formation efficiency is low and there is no feedback. Governato et al. (2004) produced a disc galaxy employing standard star formation and feedback recipes and claimed that numerical resolution is the primary cause of the angular momentum problem. Abadi et al. (2003a,b) were able to generate a galaxy resembling early-type spirals for which they calculated detailed photometric and dynamical properties. Robertson et al. (2004) adopted the multiphase model for the star-forming interstellar medium (ISM) of Springel & Hernquist (2003), which stabilizes gaseous discs against the Toomre instability, and produced a galaxy having an exponential surface brightness profile. Note that earlier work by Steinmetz & Navarro (1999) followed galaxy formation in randomly chosen haloes, while Abadi et al. (2003a) and Governato et al. (2004) selected haloes that have no major mergers at low redshift ($z < 2$ in Governato et al.). In the ΛCDM model, haloes with such quiet merger histories, while favourable for disc formation, have a number density today which is too low to account for the observed number density of spiral galaxies.

While early simulations have already included simplified treatments of chemical evolution (Steinmetz & Müller 1995; Raiteri, Villata & Navarro 1996; Berczik 1999), more recent simulations have considered Type Ia supernovae (SNe Ia) in addition to Type II supernovae (SNe II), sometimes relaxing the instantaneous recycling approximation (IRA; Lia, Portinari & Carraro 2002; Kawata & Gibson 2003; Kobayashi 2004). In particular, Kawata & Gibson (2003) have argued that the non-instantaneous nature of SNe II and SNe Ia is important for the dynamical evolution of galaxies. Brook et al. (2004) have shown that the chemical abundance of the halo stars could be an additional constraint for the modelling of feedback.

In this paper, we present a new series of simulations of galaxy formation. The main difference with previous work is that we consider an unconventional star formation model which, however, has been claimed to be required to explain the properties of high-redshift submillimetre and Lyman-break galaxies (Baugh et al. 2005), as well as the metallicity of the intracluster medium (Nagashima et al. 2005a) and of elliptical galaxies (Nagashima et al. 2005b). In this model, star formation normally proceeds in a quiescent mode with a standard initial mass function (IMF). However, when a major merger occurs, it triggers a burst of star formation with a top-heavy IMF. The distinction between quiescent and burst modes is not particularly controversial but the adoption of a top-heavy IMF is. Baugh et al. (2005) have claimed that the number density of submillimetre galaxies, in particular, is impossible to explain without a top-heavy IMF in bursts, while Nagashima et al. (2005a) have claimed that the ratio of alpha to iron peak elements in the intracluster medium can only be understood if bursts have a top-heavy IMF. A review of the observational and theoretical evidence for and against a top-heavy IMF may be found in these papers and references therein.

Our main result is that the adoption of a top-heavy IMF in bursts eases the formation of a large disc primarily because at early times, when mergers are more important, more energy per unit of mass turned into stars is made available for feedback. However, we also find that varying the criteria for a burst or varying the IMF in bursts can have a strong effect on the final morphology of the simulated galaxy.

This paper is organized as follows. We describe our simulation code and model for star formation and feedback in Section 2. We present the details of our simulations in Section 3 and the results in Section 4. Finally, in Section 5, we present a discussion and summary of our conclusions.

2 SIMULATION CODE

We use the parallel PM–TreeSPH code GADGET2 (Springel 2005), a successor of the TreeSPH code GADGET (Springel, Yoshida & White 2001). The hydrodynamics are solved using an SPH algorithm (Lucy 1977; Gingold & Monaghan 1977) and a 'conservative entropy' formulation that manifestly conserves energy and entropy (Springel & Hernquist 2002).

Here, we briefly describe modifications we have made to the code so as to adapt it for our purposes. In the conservative entropy formulation, the smoothing length of an SPH particle should be given by

$$\frac{4\pi}{3} h_i^3 \rho_i = M_{\rm ngb} = \text{constant}, \tag{1}$$

where h_i and ρ_i are the smoothing length and density of the ith SPH particle, respectively, and $M_{\rm ngb}$ represents the mass in its smoothing volume. We set $M_{\rm ngb} = 40 m_{\rm orig}$ throughout this paper, where $m_{\rm orig}$ is the original SPH particle mass. The default implementation of GADGET2 keeps the number of neighbouring particles in the smoothing volume constant, whereas we choose to keep the mass resolution constant as in equation (1). Because in our simulations the gas particle masses vary due to star formation and feedback, these two choices are not equivalent. We also adopt the phase decoupling technique introduced by Okamoto et al. (2003) to avoid spurious angular momentum transfer from cold gas discs to surrounding hot halo gas. We describe the modelling of cooling, star formation, and feedback in the following subsections.

2.1 Gas cooling

We calculate the cooling/heating rate and ionization state of each particle by assuming collisional ionization equilibrium and the presence of an evolving but uniform ultraviolet (UV) background (Haardt & Madau 1996) that is switched on at $z = 6$. Inverse Compton cooling is also included. In order to take the metallicity dependence into account, we use the appropriate cooling tables given by Sutherland & Dopita (1993) at $T > 10^4$ K. The coolest gas in overdense regions typically has a temperature $T \simeq 10^4$ K, because we do not include molecular cooling or metal cooling below 10^4 K.

Metals are carried by particles and once assigned to a particle, they remain with it. None the less, effective mixing takes place because we use the smoothed metallicity (smoothed in the same way as other SPH quantities) when computing the cooling rates.

2.2 Star formation and feedback

In general, star formation in numerical simulations is modelled as

$$\frac{{\rm d}\rho_*}{{\rm d}t} = c_* \frac{\rho_{\rm g}}{t_{\rm dyn}}, \tag{2}$$

where ρ_*, ρ_g, $t_{dyn} = (4\pi G\rho_g)^{-1/2}$ and c_* are the stellar density, the gas density, the local dynamical time and a dimensionless star formation efficiency parameter, respectively.

Typically, $c_* \simeq 1/30$ has been used in simulations of disc formation (e.g. Steinmetz & Navarro 1999; Thacker & Couchman 2001; Abadi et al. 2003a; Governato et al. 2004; Robertson et al. 2004) in order to reproduce the observed gas mass fraction and/or the Kennicutt (1998) law. Meza et al. (2003) showed that the same star formation model used by Abadi et al. (2003a) could also lead to the formation of an elliptical galaxy if the initial conditions were such that a major merger took place at low redshift. On the other hand, some simulations of elliptical galaxy formation have used large values of $c_* = 0.5 \sim 1$ (e.g. Kobayashi 2004; Kawata & Gibson 2005), often with strong feedback, in order to reproduce the observed sizes and/or colours of elliptical galaxies. Sommer-Larsen et al. (2003) combined these two star formation recipes by introducing 'early' and 'late' star formation modes. In the early star formation mode, they adopted $c_* = 1$, together with a low threshold density for star formation and very strong feedback while, in the late star formation mode, they adopted $c_* = 1/40$, and prevented any feedback. With this prescription, they were able to reproduce a wide range of morphological types in their simulations.

We consider two physically motivated star formation modes, which we call 'quiescent' and 'burst'. We model the quiescent mode as self-regulated star formation using a multiphase ISM model based on that developed by Springel & Hernquist (2003), but modified to avoid the IRA in which short-lived stars assumed to die immediately as they form. We use the same model for the burst mode, except that we adopt a shorter star formation time-scale ($c_* = 0.5$) and a flatter IMF with the intention of making self-regulation an unstable process. The motivation for these choices was discussed in Section 1.

2.2.1 *A multiphase model for star-forming gas*

Following Springel & Hernquist (2003), the dense ISM gas is pictured as a two-phase fluid consisting of cold clouds and an ambient hot phase whose energy is supplied by SNe explosions. We now briefly explain our model, including the modifications we have implemented.

In Springel & Hernquist (2003), the densities of cold clouds (ρ_c) and the hot phase (ρ_h) are related to the total gas density (ρ) as $\rho = \rho_c + \rho_h$. By considering the volume that each phase occupies, we impose the following relations

$$\frac{M_{SPH}}{\rho} = \frac{M_c}{\rho_c} + \frac{M_h}{\rho_h}, \tag{3}$$

$$M_{SPH} = M_c + M_h, \tag{4}$$

where M_{SPH}, M_c and M_h are the particle mass, mass in cold clouds and mass in the hot phase associated with the particle. We further assume the cold clouds are in pressure equilibrium with the hot ambient phase, namely

$$\rho u_{eff} = \rho_c u_c = \rho_h u_h, \tag{5}$$

where u_{eff} is the effective specific internal energy of an SPH particle, and u_c and u_h are the specific internal energies of cold clouds and hot phase.

We describe our multiphase model, first assuming the IRA, in which star formation, cloud formation by thermal instability, evaporation of clouds and heating of the hot phase by SN explosions are included. This model is almost identical to that of Springel & Hernquist (2003) except for the definition of the density of each phase and the metallicity dependence. We then show how to relax the IRA.

Star formation takes place on a star formation time-scale t_*

$$\frac{dM_*}{dt} = \frac{M_c}{t_*}, \tag{6}$$

where M_* is the stellar mass. The star formation time-scale, t_*, is taken to be compatible with equation (2); for $\rho > \rho_{th}$ we have

$$t_*(\rho) = t_*^0 \left(\frac{\rho}{\rho_{th}}\right)^{-1/2}, \tag{7}$$

where the value of t_*^0 is chosen to match the Kennicutt law (Kennicutt 1998) and ρ_{th} is a threshold density above which SPH particles become multiphase and are eligible to form stars. For $\rho < \rho_{th}$, no star formation takes place.

The short-lived stars immediately die and return mass and release energy, ϵ_{SN}, for each solar mass in stars formed, as SNe II. The heating rate arising from SNe is therefore

$$\left.\frac{d}{dt}(M_h u_h)\right|_{SN} = \epsilon_{SN}\frac{dM_*}{dt}. \tag{8}$$

We assume that SN explosions also evaporate the cold clouds, and transfer gas back into the ambient hot phase.

$$\left.\frac{dM_c}{dt}\right|_{EV} = A\frac{\epsilon_{SN}}{u_{SN}}\frac{M_c}{t_*}. \tag{9}$$

Here, A is the efficiency parameter and the specific supernova energy, $u_{SN} = \epsilon_{SN}/\beta$, where β is the mass fraction of short-lived stars. Following McKee & Ostriker (1977), the efficiency parameter has the density dependence

$$A(\rho) = A_0\left(\frac{\rho}{\rho_{th}}\right)^{-4/5}. \tag{10}$$

Finally, we assume the cold clouds form and grow through thermal instability, that is

$$\left.\frac{dM_c}{dt}\right|_{TI} = -\left.\frac{dM_h}{dt}\right|_{TI} = \frac{\Lambda_{net}(\rho_h, u_h, Z)}{u_h - u_c}\frac{M_h}{\rho_h}, \tag{11}$$

where Λ_{net} is the cooling function for gas of metallicity Z. We assume constant temperature, $T_c \simeq 1000$ K, for cold clouds. We use this instantaneous recycling approximation to fix the model parameters t_0^*, ρ_{th}, ϵ_{SN} and A_0 so as to reproduce the Kennicutt law in Section 2.2.3

2.2.2 *Removing the instantaneous recycling approximation*

We do not use the IRA in our cosmological simulations. In this section, we describe how we model feedback and chemical evolution. We assume that each stellar particle represents a single stellar population, and so star formation must be treated statistically. Using equation (6), a qualifying particle spawns a new stellar particle of mass $m_* = m_{orig}/N_g$ during a time-step Δt with probability:

$$p = \frac{M_c}{m_*}\left[1 - \exp\left(-\frac{\Delta t}{t_*}\right)\right]. \tag{12}$$

We use $N_g = 3$ and have confirmed that our results do not change for $N_g \geqslant 2$. When an SPH particle spawns a stellar particle, the mass of cold clouds is reduced by m_* and the following new specific energy u'_{eff} and new density ρ' (in the code we compute the effective entropy

instead of $u_{\rm eff}$) are given to the particle assuming the particle volume $M_{\rm SPH}/\rho$ remains constant during the time-step:

$$u'_{\rm eff} = \frac{M_{\rm SPH}u_{\rm eff} - m_* u_{\rm c}}{M_{\rm SPH} - m_*},$$

$$\rho' = \rho \frac{M_{\rm SPH} - m_*}{M_{\rm SPH}}.$$

We then update $M_{\rm SPH}$.

Each stellar particle has its own age, metallicity and IMF. We define the IMF as the number of stars per logarithmic interval of stellar mass per unit total mass of stars formed

$$\phi(m) \equiv {\rm d}N/{\rm d}\ln m \propto m^{-x}; \qquad m_l < m < m_u, \tag{13}$$

where m_l and m_u are the lower and upper mass limits of the IMF. The IMF has the following normalization:

$$\int_{m_l}^{m_u} m\phi(m){\rm d}\ln m = \int_{m_l}^{m_u} \phi(m)\,{\rm d}m = 1. \tag{14}$$

The recycled mass fraction from an evolving population of stars is a function of time. For a population of stars formed with an IMF $\phi(m)$ at time $t = 0$, the mass fraction returned to the ISM by time t is

$$E(\leqslant t) = \int_{M(t)}^{m_{\rm u}} [m - M_{\rm r}(m)]\phi(m)\frac{{\rm d}m}{m}, \tag{15}$$

where $M(t)$ is the initial mass of a star just reaching the end of its lifetime at t, and $M_{\rm r}(m)$ is the mass of the remnant left by a star with initial mass m. The lifetimes are taken from Portinari, Chiosi & Bressan (1998) for massive stars and from Marigo (2001) for intermediate- and low-mass stars.

The cumulative number of SNe II explosions up to time t (per solar mass of stars formed), $R_{\rm II}(\leqslant t)$, and the mass fraction of metals of the ith element, $E_i(\leqslant t)$, are given by

$$R_{\rm II}(\leqslant t) = \int_{\max[M(t),8\,{\rm M}_\odot]}^{m_{\rm u}} \phi(m)\frac{{\rm d}m}{m}, \tag{16}$$

$$E_i(\leqslant t) = \int_{M(t)}^{m_{\rm u}} M_i(m)\phi(m)\frac{{\rm d}m}{m}, \tag{17}$$

where $M_i(m)$ is the mass of the ith element released from a star with mass m. As E_i includes metals present when the stars formed, the pre-existing metals must be subtracted in order to estimate chemical yields, $p_i(t)$. If the metallicity of stars with respect to the ith element at their birth is Z_i^0, E_i can be divided into two terms

$$E_i(\leqslant t) = p_i(\leqslant t) + Z_i^0 E(\leqslant t), \tag{18}$$

where

$$p_i(\leqslant t) = \int_{M(t)}^{m_{\rm u}} y_i(m)\phi(m)\frac{{\rm d}m}{m}, \tag{19}$$

and $y_i(m)$ indicates the mass of the newly produced ith element in a star with mass m. Although M_i and y_i depend on the initial stellar metallicity in principle, we neglect this dependence and use the values for solar initial metallicity throughout, which are taken from Portinari et al. (1998).

We consider energy and chemical feedback from SNe Ia as well. We calculate the number of SNe Ia explosions using the scheme of Greggio & Renzini (1983), with parameters updated according to Portinari et al. (1998). The progenitors of SNe Ia are assumed to be binary systems with initial masses in the range $m_{\rm B,low} < m_{\rm B} < m_{\rm B,up}$, where $m_{\rm B} \equiv m_1 + m_2$, and m_1 and m_2 are the initial masses of the primary and secondary, respectively. We assume $m_{\rm B,up} = 2m_{1,\rm max}$, where $m_{1,\rm max}$ is the largest single-star mass for which the endpoint is a C–O white dwarf. The binary star systems that are the progenitors of SNe Ia are assumed to have an initial mass function $B\phi(m_{\rm B})$, where $\phi(m)$ is the same as for the single-star IMF. The distribution of mass fraction for the secondary, $\mu = m_2/m_{\rm B}$, is assumed to have the form (normalized over the range $0 < \mu < 1/2$)

$$f(\mu) = 2^{1+\gamma}(1+\gamma)\mu^{\gamma}. \tag{20}$$

For a single generation of stars formed at $t = 0$, the number of SNe Ia explosions up to time t is then given by

$$R_{\rm Ia}(\leqslant t) = B\int_{m_{\rm B,low}}^{m_{\rm B,up}} \phi(m_{\rm B})\left[\int_{\mu_{\rm min}(t)}^{1/2} f(\mu){\rm d}\mu\right]\frac{{\rm d}m_{\rm B}}{m_{\rm B}}, \tag{21}$$

where the lower limit

$$\mu_{\rm min}(t) = \max\left[\frac{M(t)}{m_{\rm B}}, \frac{m_{\rm B} - m_{\rm B,up}/2}{m_{\rm B}}\right] \tag{22}$$

is set by the conditions that the secondary has evolved off the main sequence and that $m_1 = m_{\rm B} - m_2 \leqslant m_{1,\rm max}$. Following Portinari et al. (1998), we adopt $m_{\rm B,low} = 3\,{\rm M}_\odot$, $m_{\rm B,up} = 12\,{\rm M}_\odot$, $\gamma = 2$ and $B = 0.07$. Finally, the yield of metals from SNe Ia is computed as

$$p_{{\rm Ia},i}(\leqslant t) = M_i^{\rm Ia} R_{\rm Ia}(\leqslant t), \tag{23}$$

where $M_i^{\rm Ia}$ is taken from the W7 model of Nomoto et al. (1997). In our code, we follow the evolution of oxygen, iron, magnesium and silicon. Because we vary the IMF, the self-consistent treatment of metals is very important, and allows us to make predictions, for example, for the abundance and abundance ratios of the α-elements to the iron-peak elements. These aspects of the simulation will be considered in a later paper.

As described above, each stellar particle returns mass, energy and metals to the ambient gas according to its age and metallicity. We smoothly distribute these quantities amongst the neighbouring gas particles using the SPH smoothing. There are various possible ways to define the smoothing length of a stellar particle. As the masses of SPH particles are variable, we choose to set the smoothing length of a stellar particle so as to have a constant mass (rather than number) within the smoothing volume. This method ensures numerical convergence if one chooses the constant mass as $M_{\rm ngb} = \alpha m_{\rm orig}$, where $M_{\rm ngb}$ is the gas mass within the smoothing volume and α is a parameter whose value should not be changed by the resolution. In general, smaller α results in stronger feedback effects as expected. As a rational choice we use the same mass resolution as in the hydrodynamic calculation, that is $\alpha = 40$. The mass ejected from evolved stars and SNe Ia is simply added to the mass of the hot phases of the neighbouring gas particles. For an SPH particle that receives an ejected mass $\Delta M_{\rm FB}$ during the time-step, we assign a new effective specific energy $u'_{\rm eff}$ and a new density ρ' according to

$$u'_{\rm eff} = u_{\rm eff}\frac{M_{\rm SPH}}{M_{\rm SPH} + \Delta M_{\rm FB}}$$

and

$$\rho' = \rho\frac{M_{\rm SPH} + \Delta M_{\rm FB}}{M_{\rm SPH}}.$$

Using equation (9), the mass evaporated by SNe is calculated according to the energy, $\Delta Q_{\rm FB}$, received during the time-step Δt

$$\Delta M_{\rm EV} = A\frac{\Delta Q_{\rm FB}}{u_{\rm SN}}, \tag{24}$$

where we compute $u_{\rm SN}$ considering only contributions from stars heavier than 8 $M_\odot$ using the IMF for the quiescent star formation mode (see Section 2.2.3).

The new mass of the hot phase, $M'_{\rm h}$, is given by solving the thermal energy equation implicitly, using equation (11)

$$M'_{\rm h} = M_{\rm h} + \Delta M_{\rm EV} - \frac{\Lambda_{\rm net}(\rho'_{\rm h}, u_{\rm h}, Z)}{u_{\rm h} - u_{\rm c}} \frac{M'_{\rm h}}{\rho'_{\rm h}} \Delta t, \tag{25}$$

where the new density of the hot phase, $\rho'_{\rm h} = \rho_{\rm h}(M'_{\rm h})$, is given by equations (3), (4) and (5) assuming $u_{\rm h}$ and the particle volume remain constant during cloud growth.

The new specific energy of the hot phase, $u'_{\rm h}$, is also calculated implicitly:

$$u'_{\rm h} = u_{\rm h} + \frac{\Delta Q_{\rm FB} + (u_{\rm c} - u'_{\rm h})\Delta M_{\rm EV}}{M'_{\rm h}}. \tag{26}$$

We impose an additional time-step criterion, $\Delta t_{\rm FB}$, for stellar particles so as to capture the non-instantaneous feature properly

$$\Delta t_{\rm FB} = \max(c_{\rm FB} t_{\rm age}, 0.5\,{\rm Myr}), \tag{27}$$

where $c_{\rm FB}$ is a parameter and $t_{\rm FB}$ is the age of a stellar population. We have confirmed that the simulation results converge for $c_{\rm FB} < 0.1$, and thus employ $c_{\rm FB} = 0.05$ throughout.

2.2.3 *Quiescent star formation mode and parameter setting*

The model described above has three parameters: the threshold density $\rho_{\rm th}$, the evaporation efficiency parameter A_0, and the characteristic star formation time-scale t^0_*. Before we can specify these parameters, we have to fix the IMF and the amount of energy released by a SN. For this quiescent mode of star formation, we use the Salpeter IMF ($x = 1.35$ in equation 13; Salpeter 1955) with $m_{\rm u} = 100\,M_\odot$ and $m_{\rm l} = 0.1\,M_\odot$ and adopt 2×10^{51} erg for the energy released per SN, which yields a SN temperature $T_{\rm SN} = 2\,\mu u_{\rm SN}/(3k) \simeq 3.3 \times 10^8$ K, where μ denotes the mean molecular weight. The reason why we use this rather than the canonical value of 10^{51} erg per SN is simply that we need this amount of energy in order to reproduce the Kennicutt (1998) law for gas with solar metallicity. For primordial gas, the value 10^{51} erg per SN is sufficient. Note that an IMF with a single slope is too simple a description (e.g. Kennicutt 1983; Kroupa 1998) and changing the slope of the low mass portion, say for $m < 1\,M_\odot$, can easily change the number of SNe II by a factor of $\sim$2. For simplicity, we restrict ourselves to using a single-slope IMF, but we reserve the freedom to increase the energy per SN just discussed.

To fix the model parameters, we considered self-regulated star formation in a self-gravitating gas sheet, adopting the IRA. This procedure is identical to that followed by Springel & Hernquist (2003), so we will give no further details here. The values of the parameters we adopt are given in Table 1.

In Fig. 1, we show the relation between the star formation surface density and the gas surface density in an idealized simulation of disc formation in a virialized halo (see Okamoto et al. 2003). Even though the values of the parameters were set assuming the instantaneous recycling approximation and solar metallicity, this simulation, which did not make this approximation and followed chemical evolution, shows reasonable agreement with the target relation. The surface gas density at the edge of star-forming region is also consistent with the threshold surface density.

Table 1. The values of the model parameters, adjusted to reproduce the Kennicutt (1998) law represented by equation (25) in Springel & Hernquist (2003).

$\rho_{\rm th}$	t^0_*	A_0
2×10^{-25} g cm^{-3}	2.8 Gyr	1300

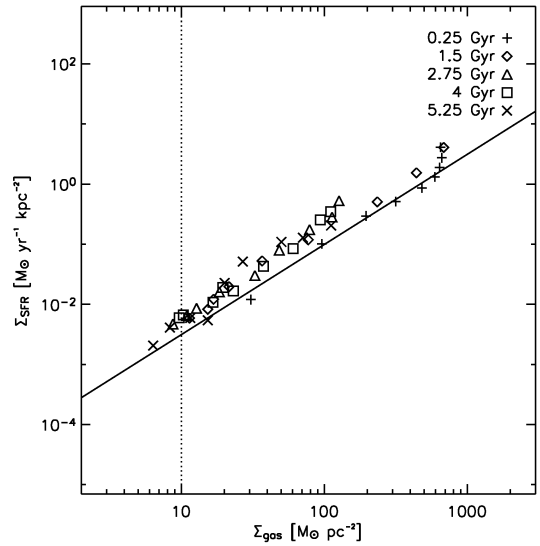

Figure 1. Star formation rate per unit area versus gas surface density in an idealized simulation of disc formation in a virialized halo. The surface star formation rate densities are computed using the surface density of stars younger than 3×10^7 yr in cylindrical bins. The outermost bin corresponds to the edge of the star-forming region. The symbols represent star formation rates at $t = 0.25$, 1.5, 2.75, 4 and 5.25 Gyr, indicated by crosses, diamonds, triangles, squares and times symbols, respectively. The solid and dotted lines indicate the target relation and the cut-off surface density, respectively.

2.2.4 *The burst mode and top-heavy IMF*

In the self-regulated star formation that occurs in the quiescent star formation mode, cooling and feedback are balanced. We implement a second mode of star formation, which is able to blow gas out of galaxies. For this to occur, the injection of feedback energy has to be more rapid. Hence, we require that star formation should occur in short bursts in physical conditions that permit heating by feedback to exceed local cooling. After various tests, we found that sufficient heating cannot be obtained simply by adopting a shorter t^*_0 (or, equivalently, a larger c_*). Motivated by the considerations discussed in Section 1, we therefore decided to assume a top-heavy IMF in the burst mode as well as a short star formation time-scale. We use $t^*_0 \simeq 0.15$ Gyr, which corresponds to $c_* = 0.5$, and an IMF with slope $x = 0.34$, which maximizes the number of SNe II. The other parameters, including the upper and lower mass limits for the IMF, are the same as for quiescent star formation.

In semi-analytical galaxy formation models, it is usually assumed that a starburst is triggered by a major galaxy merger (e.g. White & Frenk 1991; Kauffmann, White & Guiderdoni 1993; Cole et al. 2000), although some studies include small starbursts induced by minor mergers as well (Somerville & Primack 1999; Okamoto & Nagashima 2003). In our simulations, we would like to model the burst on the basis of local physical quantities rather than on global information such as the merger mass ratio, which is not easily

available. Exactly how to do this, however, is not evident. In this paper, we examine two possibilities for triggering the burst mode of star formation.

First, we consider the gas density. Mihos & Hernquist (1994) showed that cold gas is driven to the centre of the remnant when galaxies merge. The burst is therefore preceded by an increase in the central density and it seems plausible that imposing a threshold density, $\rho_{\rm burst}$, above which the burst mode is switched on, can capture the conditions under which nuclear starbursts occur in merging galaxies. In addition, Springel & Hernquist (2003) noted that self-regulation in the multiphase model breaks down at sufficiently high density; our 'density-induced' burst may be considered as a crude modelling of this process.

The second plausible trigger for bursts is the presence of shocks. Galaxy mergers induce strong, galactic-scale shocks. Indeed, Barnes (2004) suggested that shock-induced star formation is the dominant mode in interacting galaxies. We model a shock-induced burst as follows. When the rate of change of the entropy variable $K(s) \equiv (\gamma - 1)u\rho^{1-\gamma}$ due to the artificial viscosity exceeds a threshold value, $\dot{K}_{\rm burst}$, the burst mode is switched on. We use $\gamma = 5/3$ throughout. Note that other variables such as $\dot{u}$ or $\rho/(\dot{\rho}t_{\rm dyn})$ can also be used to identify shocked particles, and we have confirmed that these alternative choices produce the same results for appropriate values of the thresholds. In contrast to the density-induced burst, the shock-induced burst is expected to result in a large-scale (galactic-scale) starburst in interacting galaxies. The shock trigger is more sensitive to mergers than the density trigger because, in the latter case, the burst cannot start until sufficient gas has been funnelled into the galactic centre by the merger (Barnes 2004).

We use $\rho_{\rm burst} = 10^{-23}$ g cm^{-3} and $\dot{K}_{\rm burst} = 9 \times 10^3$ in our code units (h^{-1} Mpc, km s^{-1} and $10^{10}\,h^{-1}$ M$_\odot$ for length, velocity and mass, respectively) throughout this paper. The dependence of our results on these parameters will be discussed later. It should be noted that, for the density-induced burst, our results do not depend on resolution as long as this is good enough to resolve the threshold density $\rho_{\rm burst}$. On the other hand, the shock-induced burst will have a strong dependence on resolution because the width of the shocked layer is simply proportional to the smoothing length. Thus, we would need to adjust $\dot{K}_{\rm burst}$ or t_0^* for the burst mode if we were to change the numerical resolution.

3 SIMULATION SETUP

In order to study disc formation, we have selected from a pre-existing cosmological N-body simulation a halo with a quiet merger history. The semi-analytical model of Cole et al. (2000), applied to the merger tree of this halo, predicts a galaxy that is disc-dominated at the present day. This halo is, in fact, the same as that used in Okamoto et al. (2003). In that paper, we showed that, if cooling is not allowed to occur until $z = 1$, then a reasonable disc galaxy forms by $z = 0$.

3.1 Initial condition

We assume a low-density, flat CDM universe (ΛCDM) as the background cosmology. We adopt the following choices for the cosmological parameters: mean matter density, $\Omega_0 = 0.3$, Hubble parameter, $h \equiv H_0/100$ km s^{-1} Mpc$^{-1} = 0.7$, cosmological constant term, $\Omega_\Lambda \equiv \Lambda_0/(3H_0^2) = 0.7$, amplitude of mass fluctuations, $\sigma_8 = 0.9$, and mean baryon density, $\Omega_{\rm b} = 0.04$.

To generate our initial conditions, we use the re-simulation technique introduced by Frenk et al. (1996). The halo of interest was grown in a dark matter simulation of a $35.325\,h^{-1}$ Mpc periodic cube. Its mass is about $M_{\rm vir} = 1.2 \times 10^{12}\,h^{-1}$ M$_\odot$ within the sphere which has the virial overdensity, $\delta_{\rm vir} = 337$, at $z = 0$. The circular velocity, spin parameter and collapse redshift of this halo are $v_{\rm c}(r_{\rm vir}) = 155$ km s^{-1}, $\lambda \equiv J|E|^{1/2}/(GM^{5/2}) = 0.038$ and $z_{\rm c} \simeq 1.5$, respectively, where $z_{\rm c}$ is defined as the redshift at which the main progenitor had half the final halo mass. To generate the new initial conditions, the initial density field of the parent simulation is recreated and appropriate additional short wavelength perturbations are added in the region out of which the halo forms. In this region we also place SPH particles in the ratio of 1 : 1 with dark matter particles. The region external to this was populated with high-mass dark matter particles, the function of which is to reproduce the appropriate tidal fields. The initial redshift of the simulation is 50. The masses of the SPH and high-resolution dark matter particles are $\sim 2.6 \times 10^6$ and $\sim 1.7 \times 10^7\,h^{-1}$ M$_\odot$, respectively.

The gravitational softening lengths are kept fixed in comoving coordinates for $z > 3$; thereafter they are frozen in physical units at a value (of the equivalent Plummer softening) of $\epsilon = 0.5$ and 1 kpc for the SPH and high-resolution dark matter particles, respectively. The gravitational force obeys the exact r^{-2} law at $r > 2.8\epsilon$.

3.2 Models

To investigate the effects of the burst mode of star formation on the evolution of the galaxy, we consider three models. In the first, we do not include a burst mode. We refer to this reference case as the no-burst model. The second (the density burst model) has the density-induced burst mode and the third (the shock-burst model), the shock-induced burst mode. To study the effects of the burst mode in detail, we also consider, in Section 4.4, models with different threshold values for triggering the burst, as well as models with a combination of density-induced and shock-induced bursts.

4 RESULTS

First, we present a description of the final galaxy that forms in each simulation with a different feedback prescription, and then undertake a detailed study of the evolution in each case. In the final subsection, the burst parameters are varied in order to test the sensitivity of the simulation to these assumptions.

4.1 Galaxy properties at $z = 0$

Fig. 2 shows the stellar and gas distributions within $50\,h^{-1}$ kpc boxes centred on the galaxies at $z = 0$. The edge-on and face-on projections are selected to be perpendicular and parallel to the angular momentum vector of the stellar component within the central $10\,h^{-1}$ kpc sphere. The no-burst galaxy has a tiny stellar disc and a large population of halo stars. Visually, this galaxy is similar to the one that Abadi et al. (2003a) obtained in their simulation. It should be noted that our effective equation of state for the ISM is as stiff as that used by Robertson et al. (2004), and hence the stabilization of gas against the Toomre instability is insufficient to allow a large stellar disc to form in this particular halo. The simulation with the density-burst model produces an ellipsoidal stellar object that is slowly rotating. Due to strong feedback in the galactic centre arising from the density-induced starbursts, most of the gas is expelled from the galaxy and only a diffuse gaseous ring remains. In contrast, in the shock-burst model the number of halo stars is significantly lower and an extended disc forms in both the stellar and gaseous components. At the galactic centre, dense gas cores always exist

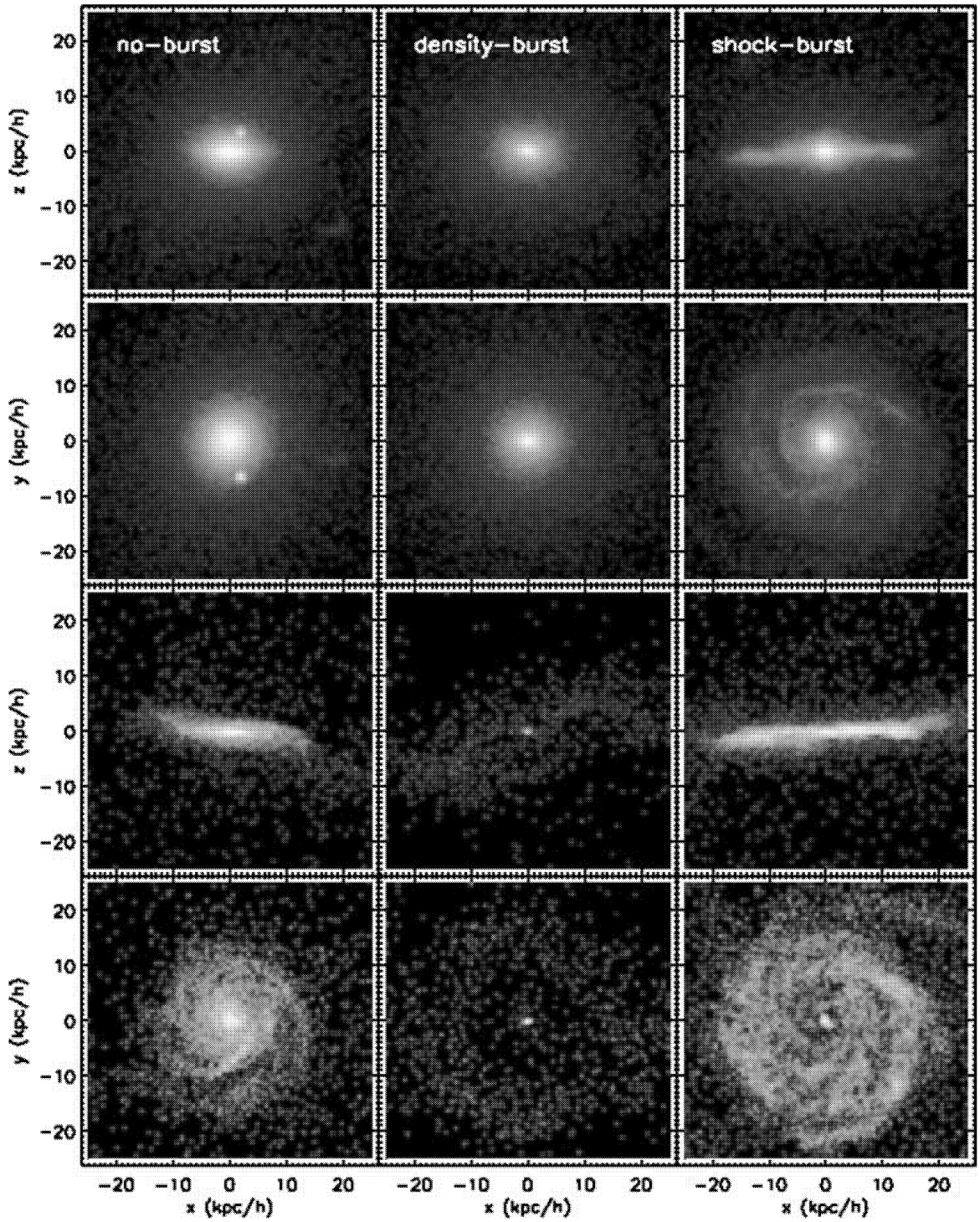

Figure 2. Galaxies at $z = 0$. The no-burst, density-burst and shock-burst models are shown from left to right. The edge-on and face-on views of stars, and edge-on and face-on views of gas are given in rows from top to bottom. We use the nett angular momentum of stars within $10\,h^{-1}$ kpc spheres to define the viewing angles. The brightness indicates the projected mass density, and the same scaling is used for each model. All of these galaxies are obtained from the same initial conditions.

regardless of the model. We suspect that this is an artificial effect caused by our limited resolution.

The *I*-band surface brightness profile of each galaxy is shown in the upper panel of Fig. 3. To compute luminosities, we used the population synthesis code PÉGASE2 (Fioc & Rocca-Volmerange 1997). The luminosity of each particle is calculated for the IMF, metallicity and age appropriate to that particle in the simulation. We fit each surface brightness profile up to 20 kpc with a double exponential because the standard $r^{1/4}$ + exponential profile cannot fit the shock-burst galaxy. It should be noted, however, that the

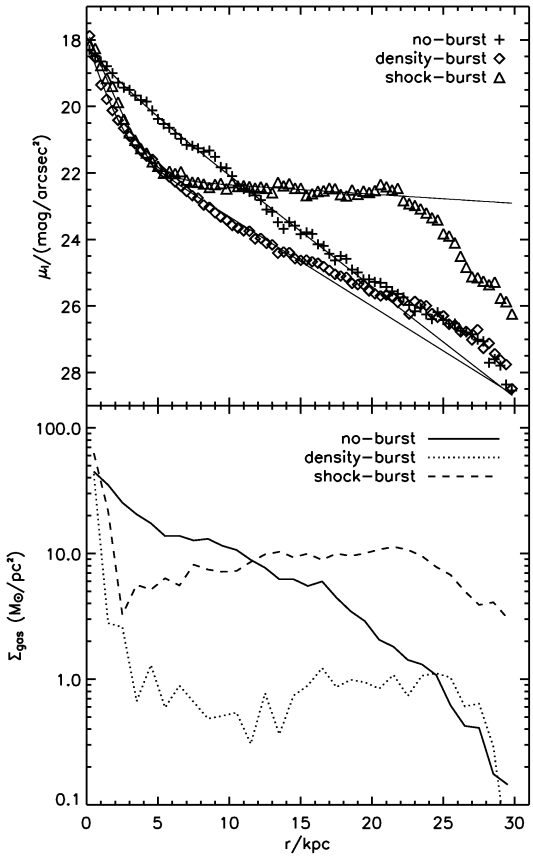

Figure 3. Upper panel: surface brightness profiles in the I band for the no-burst (crosses), density-burst (diamonds) and shock-burst (triangles) models. The solid lines are double-exponential fits for $r < 20$ kpc and the fitting parameters are given in Table 2. Lower panel: cold gas surface density profiles. The solid, dotted and dashed lines represent the no-burst, density-burst and shock-burst models, respectively. Note that we have removed the h dependence here.

$r^{1/4}$ + exponential profile is a better description for the density-burst model, and therefore the double-exponential fit underestimates its bulge. Values of the fitting parameters are shown in Table 2, which also gives the total B- and I-band luminosities of each galaxy.

The surface brightness profile of the no-burst galaxy in Fig. 3 is well fit by a single exponential (90 per cent of the I-band light comes from the outer exponential disc). Thus, there is no evidence in this profile for a bulge component even though Fig. 2 clearly shows an extended spheroidal component around this galaxy. The double exponential is a good fit to the shock-burst galaxy, but the outer exponential is rather flat, indicating that the surface brightness of the disc is nearly constant as a function of radius. The resulting scale-length, 39 kpc, is therefore very large. As we discuss in Section 5, it is possible that the disc acquires excessive angular momentum because the galactic winds are not collimated and exert a pressure on the hot gas reservoir which becomes distended and more susceptible to tidal torques at early times. In spite of its large size, the shock-burst galaxy falls on the I-band Tully–Fisher relation. For its rotation velocity of $v_{\rm rot} \simeq 200$ km s^{-1}, its absolute magnitude, $M_I = -22.7$, is only slightly brighter than the mean relation and well within the scatter (Giovanelli et al. 1997).

Table 2. Values of the parameters used in Fig. 3 to fit the I-band surface brightness profiles. The central surface brightnesses Σ^0 and the scalelengths $R^{\rm d}$ are given for the inner and outer profiles. Subscripts 'i' and 'o' indicate the inner and outer profiles, respectively. The last two columns give the total B- and I-band luminosities for each galaxy.

	$\Sigma^0_{\rm i}$	$\Sigma^0_{\rm o}$	$R^{\rm d}_{\rm i}$/kpc	$R^{\rm d}_{\rm o}$/kpc	$M_{\rm B}$	$M_{\rm I}$
No-burst	19.1	18.8	1.5	3.3	−21.1	−22.6
Density-burst	19.1	20.6	0.8	4.0	−19.7	−21.4
Shock-burst	17.7	22.1	1.0	39	−21.3	−22.7

The surface brightness profile in each galaxy reflects the cold gas surface density profile (lower panel). In the no-burst galaxy, the cold gas disc has an approximately exponential profile that is slightly more extended than the distribution of the stellar light. The density-burst galaxy has lost its gas content due to strong winds as we will show in Section 4.2. As a result, the gas surface density is an order of magnitude lower than the Kennicutt threshold ($\Sigma_{\rm gas} \simeq 10\ {\rm M}_\odot{\rm pc}^{-2}$). In the shock-burst model, a plateau is also seen in the gas surface density profile, and the surface density is close to the Kennicutt threshold. The three different models all have similar central surface gas densities. This implies that the central gas cores are a numerical artefact and higher resolution or kinetic feedback may be required to get rid of these cores.

The fits to the surface brightness profiles of Fig. 3 provide only partial information about the morphology of the galaxy. A more informative way to characterize the relative importance of bulge and disc components is to carry out the dynamical decomposition proposed by Abadi et al. (2003b). For this, we first compute the angular momentum, J_z, of each star particle parallel to the nett angular momentum of stars within $10\,h^{-1}$ kpc, and the angular momentum of the corotating circular orbit, $J_{\rm c}(E)$. The ratio $J_z/J_{\rm c}$ defines an orbital circularity. In Fig. 4, we show the probability distribution of this orbital circularity for stars within $25\,h^{-1}$ kpc of the galactic centre. A disc component should have $J_z/J_{\rm c}(E) \simeq 1$ and such a component is clearly visible in the shock-burst model, confirming the visual impression gleaned from Fig. 2. By assuming a non-rotating spheroid, i.e. that stars in the spheroid are symmetrically distributed around zero, all stars having $J_z/J_{\rm c}(E) \leqslant 0$ are identified as a half of the

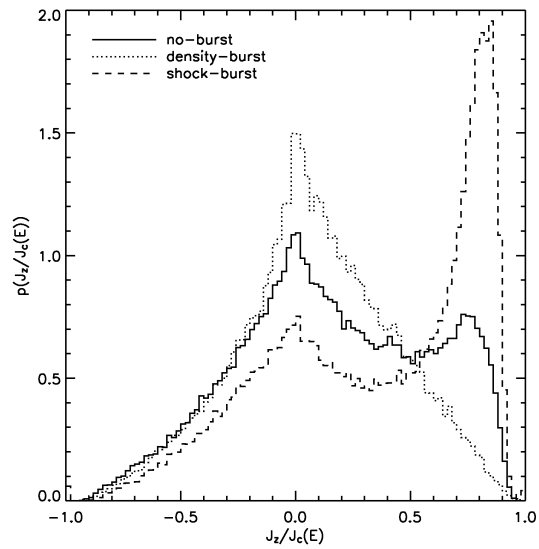

Figure 4. Mass-weighted probability distributions of the orbital circularity, $J_z/J_{\rm c}(E)$, within $25\,h^{-1}$ kpc from the galactic centre. The solid, dotted and dashed lines indicate the no-burst, density-burst and shock-burst models, respectively.

Table 3. Disc-to-total mass and luminosity ratios for the simulated galaxies at $z = 0$.

	Mass	U	B	V	I	K
No-burst	0.26	0.72	0.63	0.54	0.45	0.44
Density-burst	0.21	0.22	0.22	0.22	0.21	0.20
Shock-burst	0.48	0.86	0.84	0.80	0.72	0.66

spheroid. Their counterparts with $J_z/J_c(E) > 0$ are defined statistically. All remaining stars are identified as the disc component. We do not try to decompose the disc into thick and thin discs but defer a detailed study to a forthcoming paper.

In Table 3, we show the disc-to-total ratios for mass, U, B, V, I and K bands. The redder the band, the more the spheroid dominates. These ratios confirm that the shock-burst model has the most significant disc, while the density-burst model is the most spheroid-dominated. The B-band disc-to-total luminosity ratio of the shock-burst galaxy is $D/T = 0.84$, which is sufficiently large to be identified conventionally as a disc galaxy, while the relation between the D/T and the Hubble T-types has a large scatter (Baugh, Cole & Frenk 1996; Graham 2001). Note that the dynamical decomposition reveals a significant spheroidal component in the no-burst galaxy even though the photometric decomposition based on the surface brightness profile failed to detect it.

4.2 Mass accretion and star formation histories

The star formation histories (SFHs) of the simulated galaxies are plotted in Fig. 6 (see below). In the no-burst simulation, significant star formation activity takes place at high redshift, and this early star formation is responsible for the massive bulge (and halo) population that forms in this model. This galaxy has a nearly constant star formation rate after $z = 1$, and it builds up the tiny disc present at the final time.

The SFH of the density-burst model is similar to that of the no-burst model up to the point when the gas density reaches the threshold for a burst. At this point, the burst is triggered, the associated feedback suppresses further star formation, and the star formation rate falls well below that in the no-burst model. The huge amount of feedback energy released into a small region near the centre of the galaxy blows out most of the hot gas and this almost completely quenches further star formation. As a result, the density-induced burst simulation yields an elliptical-like galaxy. If the threshold is lowered, then the burst is turned on earlier and even fewer stars form. Thus, it is difficult to produce a galaxy that is more disc-dominated than in the no-burst case simply by allowing density-induced bursts.

By contrast, shock-induced bursts occur even at very high redshift, in small haloes where bursts are triggered both by mergers and violent collapse. The strong feedback from the stars formed in these bursts suppresses cooling and star formation during this early period when the galaxy is undergoing a number of merger events. As a result, the peak in the SFH shifts to $t \sim 5.3$ Gyr ($z \sim 1.1$). An extended reservoir of hot gas is created by the feedback energy associated with the burst and much of it remains attached to the halo. After $z = 1$, when the bulk of the dynamical activity is over, this gas cools to form an extended, young stellar disc. The key features of the shock-induced burst may be seen in the lower panel of Fig. 5. The fraction of stars born in the burst mode is large (~40 per cent) at high redshifts ($t < 6$ Gyr) and it gradually decreases to ~5 per cent towards the present. Thus, the shock-

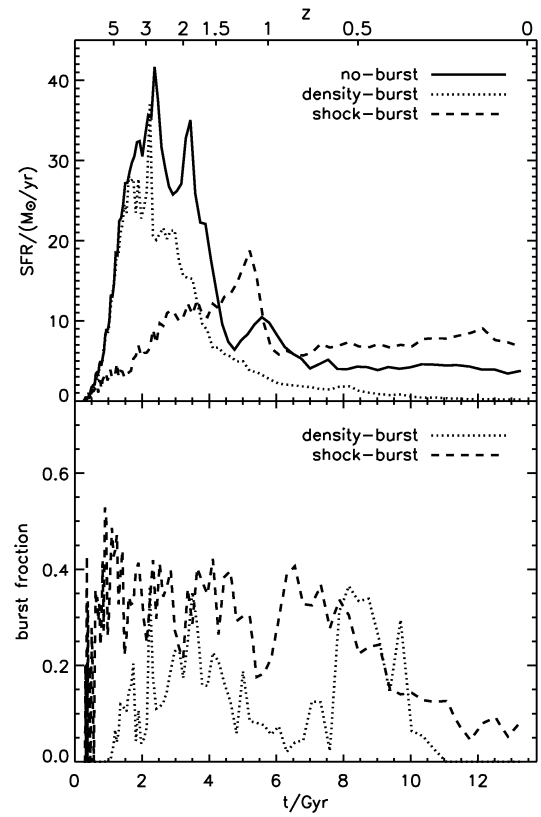

Figure 5. Upper panel: the formation history (star formation rate as a function of time) of the stars that lie within $25\,h^{-1}$kpc from the galactic centre at $z = 0$. Lower panel: the fraction of stars formed in the burst mode. The solid, dotted and dashed lines correspond to the non-burst, density-burst and shock-burst models, respectively.

burst model experiences strong feedback at early times, followed more recently by a sustained period of steady, self-regulated star formation.

The top-heavy IMF present in bursts delivers feedback energy in a particularly efficient way. It is worth noting that even at its peak, the star formation rate in the shock-burst model barely reaches $\sim 20\ \mathrm{M}_\odot \mathrm{yr}^{-1}$. However, the star formation rate in the starburst would be significantly overestimated if, as is the norm in observational studies, the rates are inferred by assuming a standard IMF.

To investigate the build-up of the visible components of the galaxy and the importance of galactic winds, we now consider the mass evolution of the main progenitor of the halo as a function of time. We define the mass of the main progenitor as $M_{\rm tot} = (4\pi/3) r_{\rm vir}^3 \rho_{\rm vir}(z)$ where $r_{\rm vir}$ is given by the spherical collapse model in our chosen cosmology (Eke, Cole & Frenk 1996). Because the accretion and cooling of baryonic matter affects the structure of the dark matter halo, the halo mass defined in this way differs slightly between models: the more concentrated the dark matter is, the smaller the halo mass. In Fig. 6, we plot the normalized main progenitor halo mass, $f_{\rm b} M_{\rm halo}/(1 - f_{\rm b})$, where $f_{\rm b} \equiv \Omega_{\rm b}/\Omega_0$ is the baryon fraction in the Universe. Also plotted are the mass of baryonic matter, $M_{\rm b}$, and the mass of cold baryons (stars and cold gas), $M_{\rm cold}$, in the main progenitor halo. If the halo had the mean cosmic baryon fraction, $f_{\rm b}$, then the normalized halo mass would be equal to the baryon mass.

The baryon fraction in the no-burst galaxy is always very close to the cosmic value. Very little gas is lost from the halo in this simulation because all the feedback energy goes mostly to support

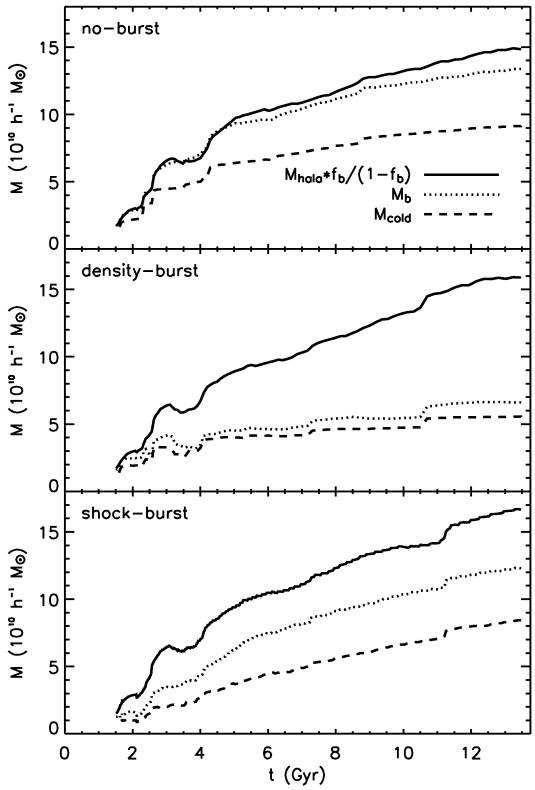

Figure 6. Evolution of the mass in the main progenitor haloes. The solid, dotted and dashed lines represent the normalized halo mass, baryon mass and the cold baryon (cold gas and stars) mass in the halo, respectively. We show the no-burst, density-burst and shock-burst models from top to bottom.

the ISM against its self-gravity. In the density-burst simulation, the baryon fraction in the halo is quite low and there is almost no hot gas left, signalling the existence of strong galactic winds. The stepwise jumps in the cold baryon mass indicate that this mass grows primarily through mergers with other haloes. The shock-burst galaxy also has winds, but these are not as strong as in the density-burst model. By the final time, the halo of the shock-burst galaxy has lost 24 per cent of its baryons. While the cold baryon content at $z = 0$ is similar to that in the no-burst simulation, the rate of growth of the cold baryons is steeper at early times in the no-burst model and at late times in the shock-burst model. This is the origin of the difference in the morphology of the final galaxy in these two cases.

The behaviour of both the SFH and the mass evolution in the shock-burst model indicates that the success of this model stems from the suppression of star formation in small haloes. In order to identify the location of the main star formation sites, we plot, in Fig. 7, the birthplaces, relative to the position of the main progenitor at the time, of the stars that end up within $25\,h^{-1}$ kpc of the galactic centre at $z = 0$. The continuous trajectories of the birthplaces in the no-burst model (top-left panel) indicate that small haloes undergo continuous star formation until they fall into the main progenitor. A similar behaviour is seen in the density-burst model. Because density-induced bursts do not occur in small haloes, where the gas density cannot reach the threshold value, star formation in such small systems is the same as in the no-burst model. The main difference between the two models is apparent in the zoomed panel on the right-hand side of the figure: strong feedback from density-induced bursts almost stops star formation in the main progenitor after $z \sim 1$. The main sites of star formation in this model are small infalling haloes. This is how the elliptical galaxy forms in the density-burst model. Unlike density-induced bursts, shock-induced bursts can occur in small haloes whose shallow potential wells make feedback particularly effective. The star formation trajectories are therefore no longer continuous. Instead, intermittent star formation in infalling haloes is clearly evident in the lower left-hand panel. As anticipated, the suppression of star formation in small galactic building blocks is the key to making a large disc.

More quantitative information on the location of the star formation sites is provided in Table 4, which lists the fraction of the final stellar mass within $25\,h^{-1}$ kpc from the galactic centre that has formed within a comoving sphere of radius $25\,h^{-1}$ kpc around the main progenitor. The mass of each star used in this calculation is the mass at $z = 0$, not the initial mass. We find that 78 per cent of the stellar mass formed in the main progenitor in the shock-burst model. In contrast, this fraction drops to 25 per cent in the case of the density-burst model.

4.3 Evolution of angular momentum

Because the direction of the angular momentum vector of the main progenitor halo varies in time due to gravitational torques, it is expected that the direction of the angular momentum vector of the accreting gas will also vary. Such a process may affect the formation of the disc through angular momentum mixing. In Fig. 8, we show the gas distribution around the main progenitor in the shock-burst model. The viewing angle is fixed and chosen so that the disc is edge-on at $z = 0$ (see the bottom-right panel of Fig. 2). A gas disc already exists at $z = 1$, but its orientation changes significantly throughout its evolution. For example, the disc is inclined and almost edge-on at $z = 1$, but it becomes almost face-on at $z = 0.7$ before settling down to the final orientation at $z = 0.2$. A good example of angular momentum mixing is seen in the panel for $z = 0.4$, where the newly accreting gas does not line up with the pre-existing inner disc but settles instead on to a different plane and the two discs torque one another. As these gas discs host star formation, this process contributes to the formation of hotter stellar components, such as a bulge or a thick disc.

In Fig. 9, we plot the evolution of the direction of the angular momentum vectors of various components of the main progenitor in the shock-burst model. The lines show the angles between each angular momentum vector and that of the final stellar disc. Angular momenta are calculated for material inside a sphere of a radius $25\,h^{-1}$ kpc (in physical coordinates) for stars (solid), cold gas (dotted) and dark matter in the core (dashed), while the angular momentum of the main progenitor halo is defined using the dark matter inside the virial radius (dot-dashed). At early times, $t < 8.5$ Gyr, the spin of the cold gas correlates well with that of the dark halo, while the stars show a better correlation with the core at $t < 6$ Gyr. Note that the angular momentum of the stellar component is contaminated by satellites and hence it is rather noisy. On the other hand, at late times, $t > 8.5$ Gyr, corresponding to $z < 0.5$, the stars follow the cold gas quite well and they are offset from both the dark matter core and halo.

We have confirmed that the angular momentum flip of the cold gas disc seen in Fig. 8 is caused by minor mergers occurring between $z \simeq 1$–0.6. Afterwards, its evolution is driven by angular momentum mixing with newly accreted gas that has a different orientation from the pre-existing disc (see Fig. 8). For the stellar component, initially the direction of its angular momentum vector is well correlated with that of the dark matter in the core, both of which result from merging

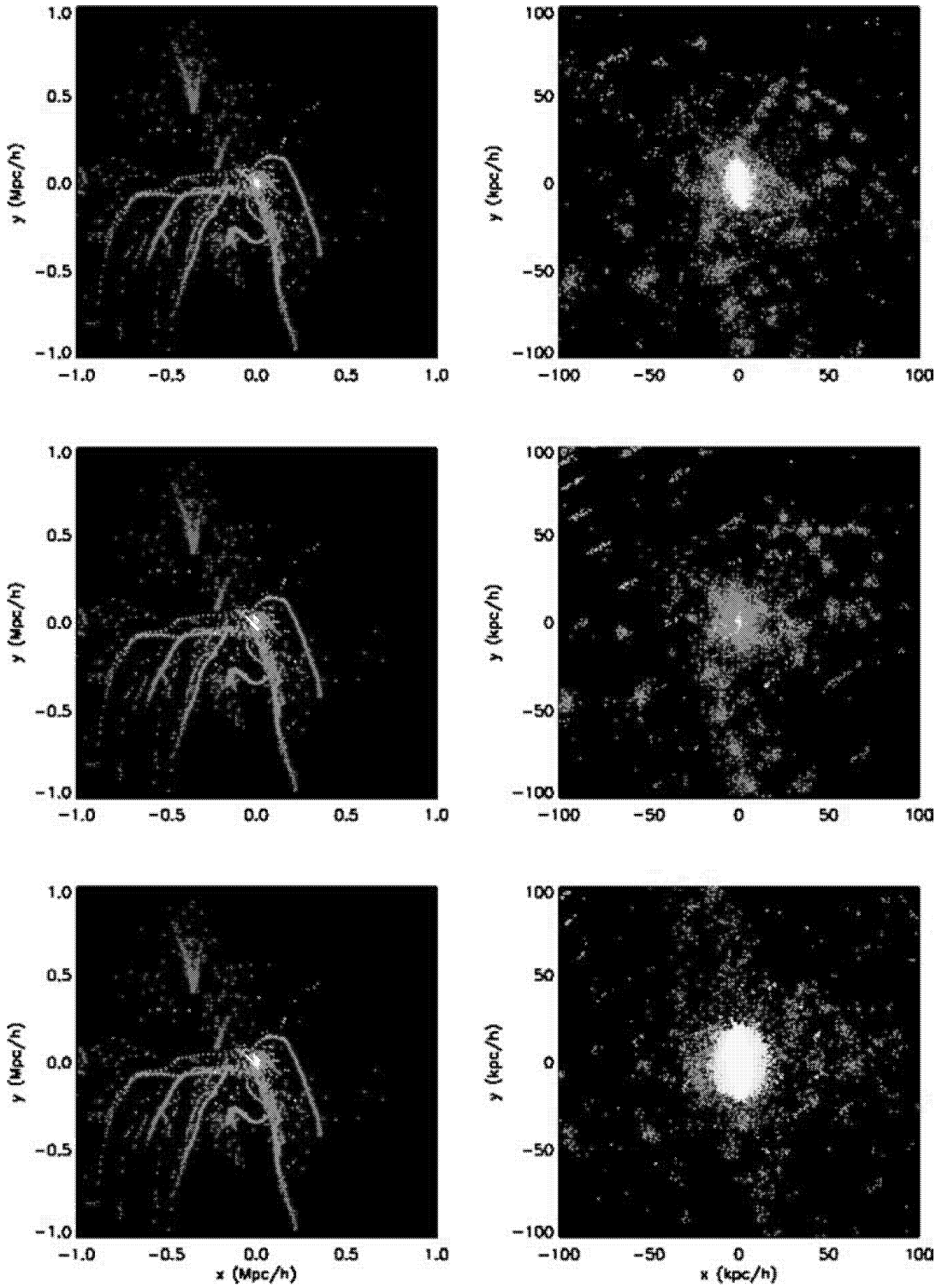

Figure 7. Birthplaces of stars that lie within $25\,h^{-1}$ kpc of the $z = 0$ galactic centre. These birthplaces are plotted relative to the position of the centre of the main progenitor at the epoch when each star forms. The brightness indicate the formation time of the stars, with the brightest being the youngest (in the online colour figure, red signifies the oldest and white the youngest). Panels show the no-burst (top row), density-burst (middle) and shock-burst (bottom) models. The left and right panels show the x–y projection of the birthplaces in 2 and $200\,h^{-1}$ kpc cubes, respectively. The coordinate system used here is that of the original simulation, i.e. it has not been rotated to match the angular momentum of the final galaxy.

and dynamical friction. As stars begin to form in the well-developed gas disc, the nett stellar angular momentum becomes dominated by disc stars, and the angular momentum vectors of the stellar and cold gas component become aligned.

4.4 Dependence on burst parameters

In this subsection, we discuss how galaxy properties are affected by changes in the burst parameters. For the shock-burst model, we

Table 4. The stellar mass formed within a comoving $25\,h^{-1}$ kpc sphere around the centre of the main progenitor divided by the total stellar mass within $25\,h^{-1}$ kpc from the galactic centre at $z = 0$.

No-burst	Density-burst	Shock-burst
0.60	0.25	0.78

have checked that if we adopt the same star formation efficiency in the burst mode as in the quiescent mode, but retain the top-heavy IMF, then the results are very similar to the no-burst simulation. Thus, a top-heavy burst IMF alone is insufficient to produce a bigger disc. Similarly, merely increasing the star formation efficiency in the burst without including a top-heavy IMF does not lead to a significantly bigger disc than is found in the no-burst simulation. Only the combination of these two features, i.e. a top-heavy burst IMF and an increased burst star formation efficiency ($c_* \sim 1$ in equation 2), is capable of promoting stronger feedback to the extent that an extended disc can form in this particular halo.

Because the response of the density-burst model to changes in the density threshold is fairly straightforward and the shock-burst model looks more promising, we decided to explore the following three additional models:

(i) SH – the same as the shock-burst model, but with a slightly higher threshold for the burst, $\dot{K}_{\rm burst} = 10^4$, rather than $\dot{K}_{\rm burst} = 9 \times 10^3$ as in the standard shock-burst model;
(ii) SL – the same as the shock-burst model, but with a lower threshold for the burst, $\dot{K}_{\rm burst} = 8 \times 10^3$;
(iii) DS – a combination of density-induced and shock-induced burst modes, with the same parameters as the original models.

In Fig. 10, we show the SFHs of the galaxies in these three variant models. Models with shock-induced bursts are quite sensitive to the threshold, $\dot{K}_{\rm burst}$. In general, the lower the threshold, the fewer the number of stars that form because of the additional amount of feedback generated by the burst stars. The DS model shows interesting behaviour. As the feedback from the shock-induced bursts suppresses gas cooling at early times, the redshift at which the gas density reaches the threshold for a density-induced burst is reduced. At this time, the depth of the potential well is deeper and this decreases the strength of galactic winds. As a result, when the density-induced bursts start, the star formation rate exceeds that in the shock-burst model. These density-induced bursts in the DS model do not lead to a smaller final bulge mass, but do suppress further cooling, showing how difficult it is to promote disc formation when a large amount of feedback energy is pumped into the galactic centre after $z \sim 2$.

Edge-on views of the final galaxies are shown in Fig. 11. Shock-induced bursts assist disc formation and lowering the threshold for such bursts results in a larger disc. Of course, too low a threshold is counterproductive. For example, for $\dot{K}_{\rm burst} = 5 \times 10^3$, the star formation becomes dominated by the burst mode at all times. As a result, only a very dim object forms because the threshold is below the typical values in the accretion shock and most of the stars are then formed outside the central disc. The galaxy in the DS model has an outer gas ring. One might suspect that this is just gas swept out by feedback. In fact, the ring is newly accreted gas that had a different angular momentum direction relative to that of the inner disc. When the outer ring is either spatially separated from the inner disc or perpendicular to it, it tends to be stable. From our experience, such outer rings are not rare in cosmological simulations because the direction of the angular momentum of the main progenitor halo can change dramatically, as we have shown in Fig. 9, and so the orientation of newly accreting gas can differ from that of the pre-existing disc (see Fig. 8).

We also performed a dynamical decomposition for these galaxies (see Table 5). As expected, lowering the threshold for a shock-induced burst leads to larger disc-to-total ratios. These numbers also confirm that density-induced bursts result in early-type galaxies even when they are combined with shock-induced bursts.

5 SUMMARY AND DISCUSSION

We have performed cosmological simulations of galaxy formation in a CDM halo chosen to have a quiet merger history. We have employed a multiphase description of the ISM based on that of Springel & Hernquist (2003) and developed explicit models for star formation in quiescent and burst modes. We assume that the star formation efficiency is much higher in the burst mode than in the quiescent mode and, motivated by the semi-analytical work of Baugh et al. (2005), that the stars in a burst form with a top-heavy IMF. Our model potentially provides a unified picture of star formation in galaxies of all morphological types. In this paper, we have explored two triggers for the starburst mode: strong shocks and a high density. An important conclusion of our work is that, for the same initial conditions, different burst models result in galaxies with a wide range of morphological types, having bulge-to-total B-band luminosities spanning the range $D/T \sim 0.2$ to 0.9.

Although, having simulated galaxy formation in only one halo, we must be cautious about generalizing our conclusions, the shock-induced burst model does look promising for creating disc-dominated galaxies in haloes with relatively quiet recent merger histories. The lower the threshold for shock-induced bursts, the more the galaxy becomes disc-dominated. The key to the success of this model in a universe where structure grows hierarchically is that the burst fraction is high at early times and subsequently decreases, once the main phase of halo merging activity has taken place. Feedback from the top-heavy IMF in the shock-induced bursts suppresses the early collapse of baryons in small haloes, helping to create a reservoir of hot gas that remains attached to the halo and is available for cooling later on. It is this gas that eventually ends up forming a large, young stellar disc in which stars continue to form at a slow rate up to the present day.

In spite of its success in generating a disc-dominated galaxy which falls on the I-band Tully–Fisher relation, our shock-induced burst model produced an excessively large disc with an unrealistically flat surface density profile. A possible cause of this problem may be the lack of collimation of the galactic winds in the simulation. The pressure generated by the roughly isotropic winds causes the hot gas reservoir to become more extended than the dark matter distribution at early times and thus susceptible to gaining extra angular momentum from tidal torques. When this gas later cools, it settles on to a disc with too much angular momentum. Thus, far from having too little angular momentum as most previously simulated discs, our disc ended up with too much angular momentum. If this interpretation is correct, the lack of collimation in the winds might just reflect the inability of SPH to represent the steep pressure gradients required to collimate the outflow. We intend to test this hypothesis with simulations using a mesh-based hydrodynamic code. This result cautions about the general assumption that the baryonic matter has the same specific angular momentum of the dark matter (Fall & Efstathiou 1980). In fact, feedback is able to change the distribution

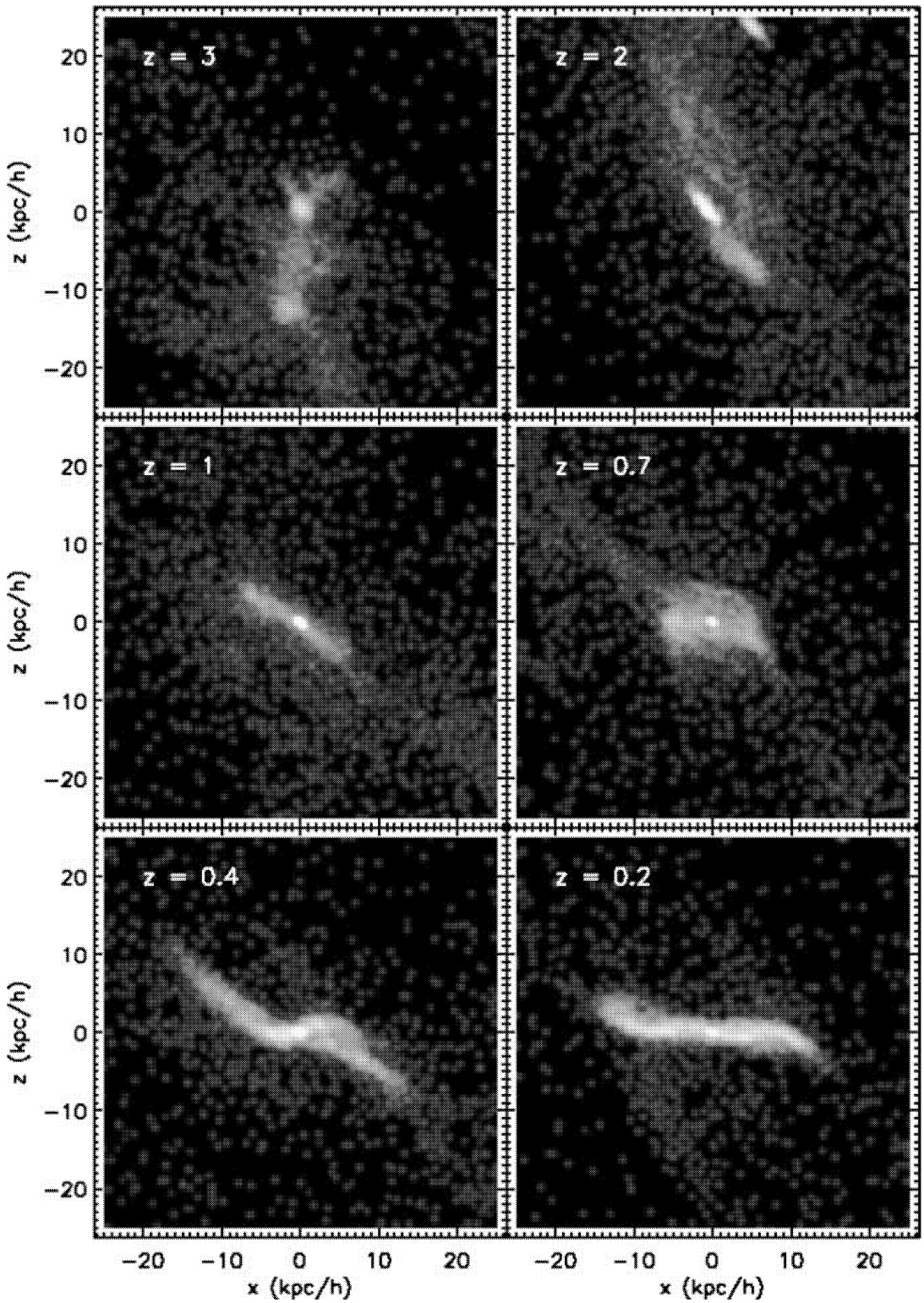

Figure 8. Gas distribution in physical $50\,h^{-1}$ kpc boxes centred on the main progenitors in the shock-burst model. A fixed viewing angle is used, that for which the disc is edge-on at $z = 0$. The $z = 0$ gas distribution is plotted in the bottom-right panel of Fig. 2.

of the gas in protogalactic regions, and therefore baryons can have higher angular momentum than dark matter.

While other improvements implemented in our simulations, such as the phase-decoupling method to suppress numerical transfer of angular momentum, high resolution, and the use of a stiff equation of state for the ISM, also contribute to the formation of large discs (see Okamoto et al. 2003; Governato et al. 2004; Robertson et al. 2004), the comparison between models with and without shock-induced

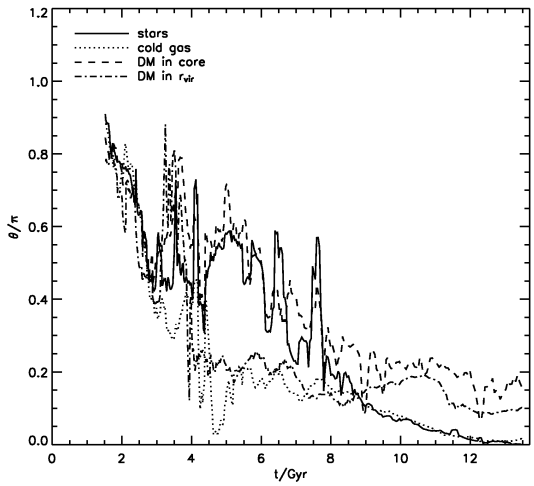

Figure 9. Evolution of the angles between the angular momentum vector of the stellar component within $10\,h^{-1}$ kpc at $z = 0$ and the angular momentum vectors of various components in the main progenitor for the shock-burst simulation. The different lines refer to the following components of the main progenitors: stars within $25\,h^{-1}$ kpc (solid), cold gas within $25\,h^{-1}$ kpc (dotted), dark matter within $25\,h^{-1}$ kpc (dashed), and dark matter within the virial radius (dot–dashed). Angles are divided by π, and $\theta/\pi = 1$ means counter-rotation relative to the final disc.

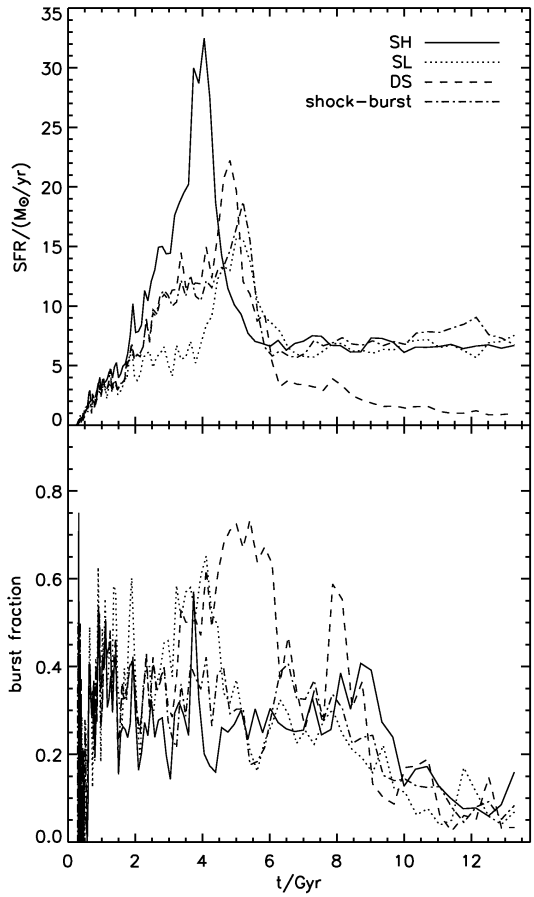

Figure 10. The same as Fig. 5 but for the SH (solid), SL (dotted) and DS (dashed) models. The standard shock-density model is also shown for comparison (dot-dashed).

bursts shows that our burst model is the key ingredient that helps resolve the angular momentum problem in a CDM universe. Although the assumption of a top-heavy IMF in bursts is controversial, it is encouraging that the model we have used is the same as was originally introduced in order to account for the abundance and properties of galaxy populations at high redshift (Baugh et al. 2005), and was subsequently found also to provide a plausible explanation for the metal content in the intracluster medium (Nagashima et al. 2005a) and in elliptical galaxies Nagashima et al. (2005b).

By contrast, the density-induced burst model seems to make things worse for disc formation. Because the gas density only reaches the threshold for bursts in massive haloes, this model does not affect gas cooling and star formation in small haloes. The feedback associated with the burst merely halts star formation in the galaxy at late times when an extended stellar disc might otherwise be expected to form. Consequently, the density-induced burst leads to the formation of an early-type galaxy. The effects of bursts (with their top-heavy IMF) in this model may resemble those generated by energy fed back from active galactic nuclei (AGN). While AGN do not produce stars and metals, both forms of feedback inject large amounts of energy into the galactic centre. Thus, we suspect that it is difficult to solve the angular momentum problem in simulations of disc galaxies solely by including AGN feedback. Of course, it is entirely possible that AGN feedback behaves quite differently from the case of density-induced bursts (see Di Matteo, Springel & Hernquist 2005; Kawata & Gibson 2005 for attempts at modelling AGN feedback on galactic scales). However, if feedback from AGN does have similar consequences to those produced by the density bursts in our simulations, then one might expect that it is particularly important for suppressing recent star formation in the most massive galaxies. This is in qualitative agreement with the observation that the most massive galaxies tend to be ellipsoidal and not disc-like.

The morphologies of galaxies formed in the simulations with shock-induced bursts are rather sensitive to the value of the burst threshold $\dot{K}_{\rm burst}$, as shown in Section 4.4, because the allowed range for this parameter is very narrow. With too low a threshold, the star formation is dominated by the burst mode at all times, and vice versa. As a result, the allowed range for $\dot{K}_{\rm burst}$ is less than an order of magnitude in our simulations. Within this range, the behaviour of the shock-burst models is easily understood. Lower threshold values suppress star formation more effectively at high redshift. Interestingly, the three shock-burst models have almost the same star formation rate at low redshift, when no major mergers occur. Because our current modelling of shock-induced bursts is not resolution-independent as we discussed in Section 2.2.4, we will explore alternative formulations in future work.

Several important tests of our model are possible and we intend to pursue these in future work. For example, we have followed in detail the evolution of the metallicity of gas and stars in our simulations, keeping track of metals produced in the quiescent and burst modes. Comparing the resulting distributions of heavy elements in the different dynamical components of the simulated galaxies with observational data will be an important test of the validity of our feedback models. A key question is how often do shock-induced bursts like those we have modelled lead to the formation of disc-dominated galaxies. Answering this question will require simulating galaxy formation in large volumes. The results presented in this paper encourage us to believe that such demanding calculations are worth pursuing.

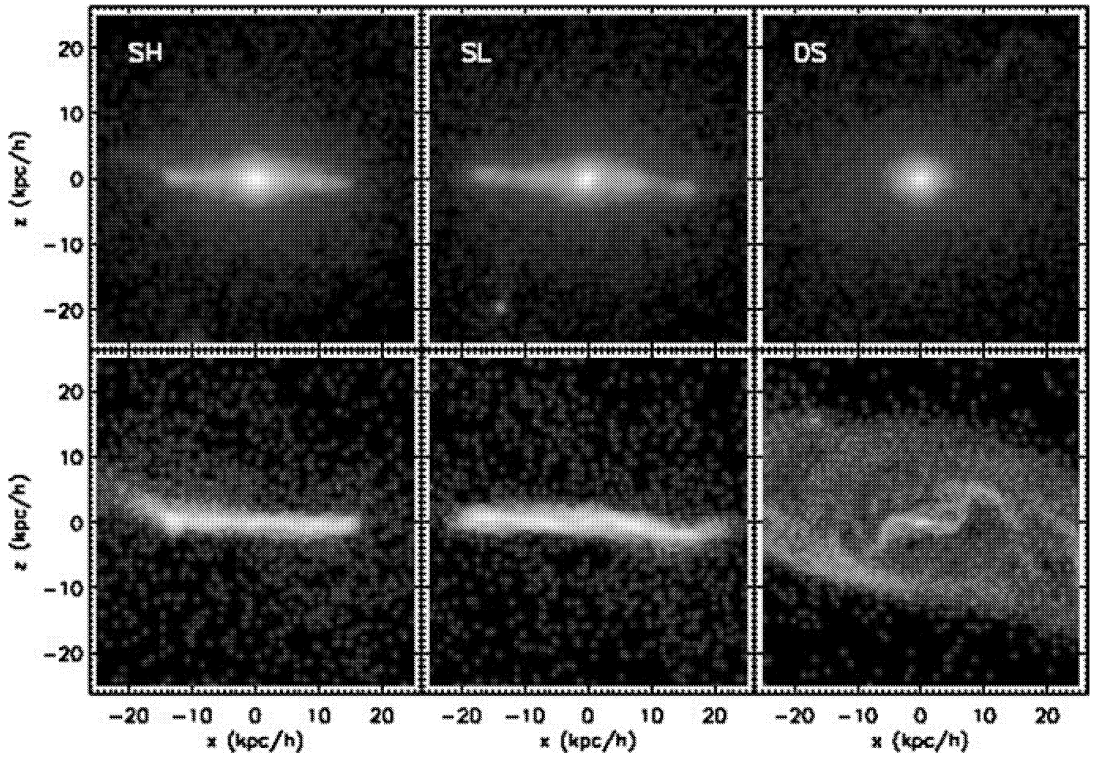

Figure 11. Edge-on projections of stars (upper row) and gas (lower row) in the SH, SL and DS models at $z = 0$.

Table 5. Disc-to-total ratios as in Table 3, only this time for galaxies in the SL, SH and DS models.

	Mass	*U*	*B*	*V*	*I*	*K*
SH	0.39	0.83	0.80	0.76	0.66	0.59
SL	0.55	0.94	0.91	0.87	0.79	0.73
DS	0.20	0.51	0.47	0.41	0.33	0.28

ACKNOWLEDGMENTS

We are grateful to Volker Springel for providing us with the GADGET2 code. We also thank Masahiro Nagashima who made look-up tables for chemical evolution. The simulations were performed on the Cosmology Machine at the Institute for Computational Cosmology in the University of Durham. This work was supported by a UK Particle Physics and Astronomy Research Council (PPARC) rolling grant for Extragalactic Astronomy and Cosmology. TO is a Research Fellow of the Japan Society for the Promotion of Science (No. 01891). VRE acknowledges a Royal Society University Research Fellowship.

REFERENCES

Abadi M. G., Navarro J. F., Steinmetz M., Eke V. R., 2003a, ApJ, 591, 499
Abadi M. G., Navarro J. F., Steinmetz M., Eke V. R., 2003b, ApJ, 597, 21
Barnes J. E., 2004, MNRAS, 352, 589
Baugh C. M., Cole S., Frenk C. S., 1996, MNRAS, 283, 1361
Baugh C. M., Lacey C. G., Frenk C. S., Granaot G. L., Silva L., Bressan A., Benson A. J., Cole S., 2005, MNRAS, 356, 1191
Berczik P., 1999, A&A, 348, 371
Brook C. B., Kawata D., Gibson B. K., Flynn C., MNRAS, 349, 52
Cole S., Lacey C. G., Baugh C. M., Frenk C. S., 2000, MNRAS, 319, 168
Di Matteo T., Springel V., Hernquist L., 2005, Nat, 433, 604
Eke V. R., Cole S., Frenk C. S., 1996, MNRAS, 282, 263
Eke V. R., Efstathiou G., Wright L., 2000, MNRAS, 315, L18
Fall S. M., Efstathiou G., 1980, MNRAS, 193, 189
Fioc M., Rocca-Volmerange B., 1997, A&A, 326, 950
Frenk C. S., White S. D. M., Efstathiou G., Davis M., 1985, Nat, 317, 595
Frenk C. S., Evrard A. E., White S. D. M., Summers F. J., 1996, ApJ, 472, 460
Gingold R. A., Monaghan J. J., 1977, MNRAS, 181, 375
Giovanelli R., Haynes M. P., Herter T., Vogt N. P., Wegner G., Salzer J. J., da Costa L. N., Freudling W., 1997, AJ, 113, 22
Governato F. et al., 2004, ApJ, 607, 688
Graham A. W., 2001, AJ, 121, 820
Greggio L., Renzini A., 1983, A&A, 118, 217
Haardt F., Madau P., 1996, ApJ, 461, 20
Katz N., 1992, ApJ, 391, 502
Katz N., Gunn J. E., 1991, ApJ, 377, 365
Kauffmann G., White S. D. M., Guiderdoni B., 1993, MNRAS, 264, 201
Kawata D, Gibson B. D., 2003, MNRAS, 340, 908
Kawata D., Gibson B. D., 2005, MNRAS, 358, L16
Kennicutt R. C., 1983, ApJ, 272, 54
Kennicutt R. C., 1998, ApJ, 498, 541
Kobayashi C., 2004, MNRAS, 347, 740
Kroupa P., 1998, MNRAS, 298, 231
Lia C., Portinari L., Carraro G., 2002, MNRAS, 330, 821
Lucy L. B., 1977, AJ, 82, 1013
McKee C. F., Ostriker J. P., 1977, ApJ, 218, 148
Marigo P., 2001, A&A, 370, 194
Meza A., Navarro J. F., Steinmetz M., Eke V., 2003, ApJ, 590, 619
Mihos J. C., Hernquist L., 1994, ApJ, 425, L13
Nagashima M., Lacey C. G., Baugh C. M., Frenk C. S., Cole S., 2005a, MNRAS, 358, 1247
Nagashima M., Lacey C. G., Okamoto T., Baugh C. M., Frenk C. S., Cole S., 2005b, MNRAS, 363, L31
Navarro J. F., Benz W., 1991, ApJ, 380, 320
Navarro J. F., White S. D. M., 1994, MNRAS, 267, 401

Navarro J. F., Frenk C. S., White S. D. M., 1995, MNRAS, 275, 56
Nomoto K., Iwamoto K., Nakasato N., Thielemann F.-K., Brachwitz F., Tsujimoto T., Kubo Y., Kishimoto N., 1997, Nucl. Phys. A, 621, 467
Okamoto T., Nagashima N., 2003, ApJ, 587, 500
Okamoto T., Jenkins A., Eke V. R., Quilis V., Frenk C. S., 2003, MNRAS, 345, 429
Portinari L., Chiosi C., Bressan A., 1998, A&A, 334, 505
Raiteri C. M., Villata M., Navarro J. F., 1996, A&A, 315, 105
Robertson B., Yoshida N., Springel V., Hernquist L., 2004, ApJ, 606, 32
Salpeter E. E., 1955, ApJ, 121, 161
Sommerville R. S., Primack J. R., 1999, MNRAS, 310, 1087
Sommer-Larsen J., Dolgov A., 2001, ApJ, 551, 608
Sommer-Larsen J., Gelato S., Vedel H., 1999, ApJ, 519, 501
Sommer-Larsen J., Götz M., Portinari L., 2003, ApJ, 596, 47
Springel V., 2005, MNRAS, submitted (astro-ph/0505010)
Springel V., Hernquist L., 2002, MNRAS, 333, 649
Springel V., Hernquist L., 2003, MNRAS, 339, 289
Springel V., Yoshida N., White S. D. M., 2001, NewA, 6, 79
Steinmetz M., Müller E., 1995, MNRAS, 276, 549
Steinmetz M., Navarro J. F., 1999, ApJ, 513, 555
Sutherland R. S., Dopita M. A., 1993, ApJS, 88, 253
Thacker R. J., Couchman H. M. P., 2001, ApJ, 555, L17
Weil M. L., Eke V. R., Efstathiou G., 1998, MNRAS, 300, 773
White S. D. M., Frenk C. S., 1991, ApJ, 379, 52

This paper has been typeset from a TEX/LATEX file prepared by the author.